Chemical
Science

Accepted Manuscript

This article can be cited before page numbers have been issued, to do this please use: Z. Ba, J. Tang, J. Zhang and C. Wang, *Chem. Sci.*, 2026, DOI: 10.1039/D6SC02576E.

Chemical
Science

Volume 9
Number 1
7 January 2018
Pages 1-268

rsc.li/chemical-science

ISSN 2041-6539

ROYAL SOCIETY
OF **CHEMISTRY**

EDGE ARTICLE
Xinjing Tang *et al.*
Caged circular siRNAs for photomodulation of gene expression in cells and mice

ROYAL SOCIETY
OF **CHEMISTRY**

rsc.li/chemical-science

View Article Online
DOI: 10.1039/D6SC02576E

ARTICLE

Membrane Anchoring Amplifies Intracellular Catalysis of Caged Palladium Nanoclusters

Zhengnuo Ba,[†a] Jiadong Tang,[†a] Junji Zhang,*[b] Chen Wang*[a]

Received 00th January 20xx,
Accepted 00th January 20xx

DOI: 10.1039/x0xx00000x

Palladium nanoclusters (Pd NCs) represent a promising candidate for intracellular redox catalysis owing to their capacity to generate reactive oxygen species (ROS). Yet, in living systems, their catalytic performance is severely constrained by rapid cytosolic passivation and the spatial mismatch between ROS production sites and biological targets. Here, we report a membrane-confined catalytic strategy that reprograms intracellular Pd nanocatalysis at the cell membrane interface. Ultrasmall molecular cage-templated Pd NCs are stably anchored within the plasma membrane via a liposome-mediated membrane fusion approach, establishing a confined reaction microenvironment. Membrane confinement not only protects catalytic active sites from cytosolic nucleophiles but also localizes ROS generation directly at the lipid bilayer, enabling efficient ROS accumulation at substantially reduced Pd dosages. The localized ROS further induce spatially lipid peroxidation and prodrug activation, establishing a membrane-level cooperative effect that boosts therapeutic efficacy. This work identifies membrane confinement as a general strategy to stabilize metal nanocatalysts and spatially program intracellular ROS reactions, providing a new framework for interface-directed regulation of cell fate.

Introduction

Metal nanoclusters (NCs) have attracted considerable interest owing to their remarkable catalytic efficiency and enzyme-mimicking activities, particularly in the context of intracellular catalytic therapy[1-9]. Among them, ultrasmall palladium nanoclusters (Pd NCs) exhibit robust catalytic turnover and enhanced catalytic activity arising from their high specific surface area[10-16], representing one of the most powerful classes of abiotic nanocatalysts. Their catalytic properties can be harnessed to generate reactive oxygen species (ROS) in a controlled manner, thereby sustaining/amplifying oxidative reactions within biological environments and offering unique opportunities for intracellular catalytic intervention[17-24]. In Pd-based catalytic systems, multiple ROS can be generated on the surface of Pd nanocrystals through distinct catalytic pathways. For peroxidase (POD)-mimicking activity, Pd surface adsorbs and cleaves H_2O_2 to generate surface-bound OH intermediates, which subsequently release •OH radicals into the solution[25]. For oxidase (OXD)-mimicking activity, Pd nanocrystals activate molecular oxygen (O_2) via dissociative adsorption to form surface O* species, which then oxidize substrates and produce H_2O_2. For catalase (CAT)-mimicking activity, the Pd surface catalyzes the decomposition of H_2O_2 into H_2O and O_2, primarily following a pathway involving H_2O_2 adsorption, O–O bond cleavage, formation of O and OOH intermediates, and O_2 desorption[26]. Notably, nanozymes with exposed Pd(111) and Pd(100) dual active centers could undergo a cascade catalytic reaction, the Pd(111) facet exhibits CAT-like activity to decompose H_2O_2 into O_2, while the Pd(100) facet subsequently displays OXD-like activity to convert O_2 into $O_2^{\bullet-}$[20]. In addition, glutathione peroxidase (GPx)-mimicking activity of Pd converts GSH to GSSG[14, 20].

However, achieving precise control over Pd NCs catalytic activity and ROS generation under physiological conditions remains highly challenging. In most reported systems, Pd NCs rely on cellular uptake and intracellular localization to exert their functions. However, their catalytic activity is often severely passivated by nucleophiles and thiol-containing biomolecules abundant in the cellular milieu[27-30]. Moreover, the effective utilization of ROS is intrinsically limited by their extremely short half-lives (1 μs – 1 ms) and limited diffusion distances (< 20 nm)[31-33], posing a fundamental barrier to the spatiotemporal regulation of ROS production and proximity to their biological targets. Without precise spatial confinement, ROS generated in bulk cytosol are rapidly quenched before exerting meaningful biological effects, resulting in low efficiency and poor controllability. Thus, overcoming catalytic passivation while simultaneously localizing ROS production is a prerequisite for enabling effective intracellular metal nanocatalysis.

Recently, spatially confined chemical transformations at plasma membrane interfaces have emerged as a powerful strategy to enhance local reaction efficiency[34-38], selectivity[39-40], as well as spatiotemporal precision[41-43], offering an alternative reaction space for modulating biological processes and directing cell fate. Inspired by this concept, anchoring ultrasmall Pd NCs at plasma membrane represents an attractive approach to fully exploit their catalytic potential by shielding them in a relatively "clean" environment, enabling localized ROS generation at the membrane interface. Achieving this goal, however, requires the concurrent realization of precise Pd NCs size control, stable membrane anchoring, and the engineering of enzyme-mimicking activities for spatially controlled ROS production. Regretfully, a general and robust strategy for integrating catalytically active Pd NCs into the plasma membrane has not yet been established.

Herein, we developed a membrane-confined catalytic system that stably anchors caged Pd NCs within the plasma membrane via a liposome-mediated fusion strategy (Scheme 1

---

[a] School of Chemistry and Molecular Engineering, East China Normal University, Shanghai 200241, China. E-mail: cwang@chem.ecnu.edu.cn
[b] School of Chemistry and Molecular Engineering, East China University of Science & Technology, 130 Meilong Road, Shanghai, 200237, China. E-mail: zhangjunji@ecust.edu.cn

† These authors contribute equally.

and Figure 1a). Pd NCs synthesized through a molecular cage-template approach exhibit well-defined ultrasmall sizes and high catalytic activity, encompassing multiple enzyme-mimicking activities, including POD-, OXD-, CAT-, and GPx-like activities. Their ultrasmall dimensions enable efficient incorporation into AS1411 aptamer-functionalized liposomes, which subsequently fuse with the cell membrane. Spatial confinement of Pd NCs at the membrane interface through this fusion strategy not only shields them from intracellular deactivation but also preserves substrate accessibility, amplifying local reaction efficiency and promoting ROS accumulation at substantially reduced Pd dosages (ca. 1/5 of that used for endocytosis). The localized ROS induces membrane lipid peroxidation and GPX4 down-regulation in tumor cells, triggering programmed cell death and enhancing therapeutic efficacy. Moreover, membrane-confined ROS allows precise control over prodrug activation. This work demonstrates that membrane confinement unlocks the full catalytic potential of Pd NCs, directly coupling metal-catalyzed chemistry with membrane lipid peroxidation and prodrug activation, revealing a new paradigm in which membrane-confined nanoscale catalysis is harnessed for precise regulation of redox signaling and cell fate.

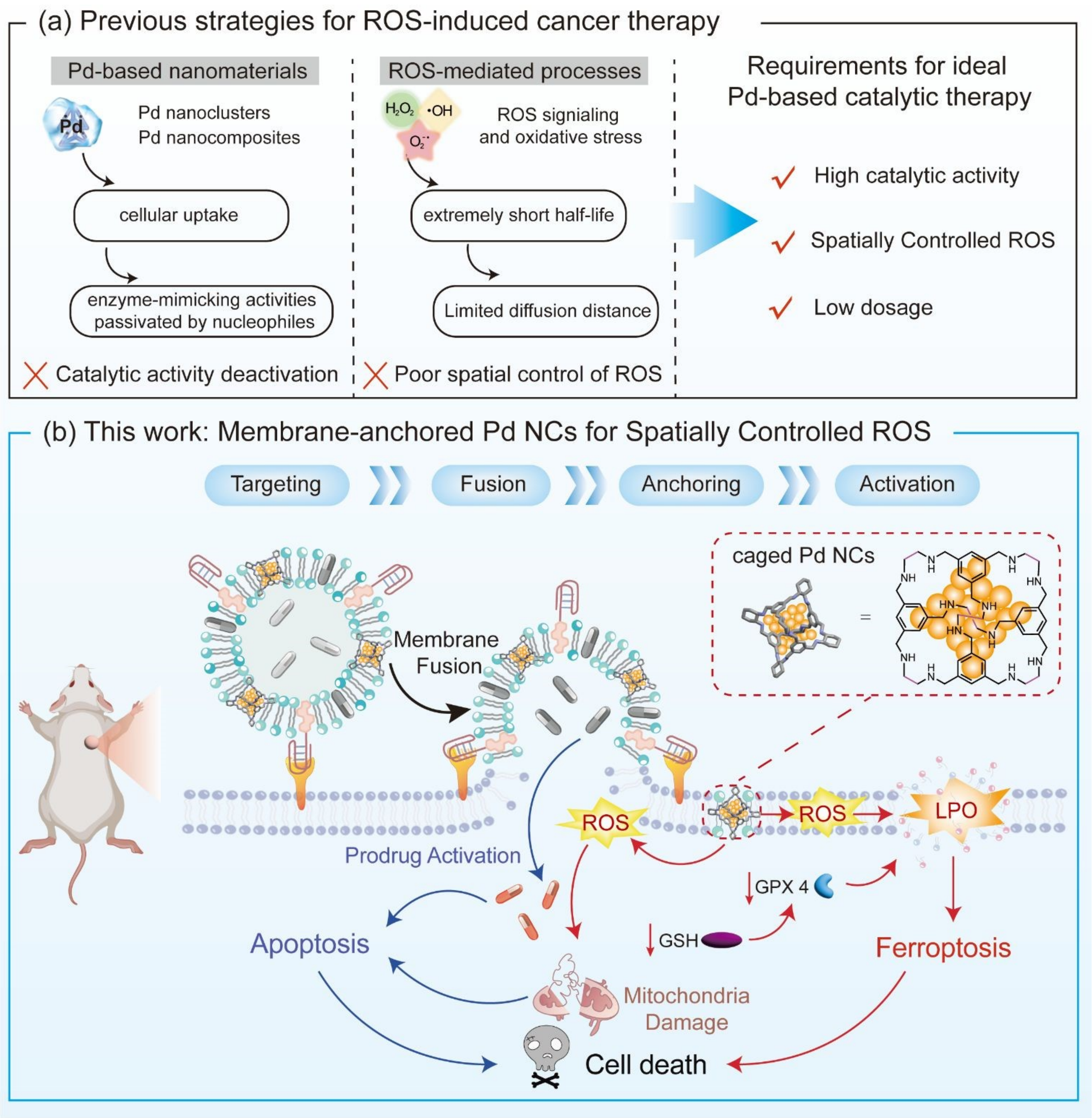

Scheme 1 (a) Reported Strategies for Cancer Therapy. (b) Schematic Illustration of the Current Strategy for Spatiotemporal-Controlled Lipid Peroxidation and Prodrug Activation via Membrane Fusion.

View Article Online
DOI: 10.1039/D6SC02576E

Results and Discussion

To precisely obtain ultrasmall and structurally well-defined palladium nanoclusters (Pd NCs), we employed molecular cage RCC3 as a confined nanospace. Using a two-solvent protocol, palladium acetate ($Pd(OAc)_2$) precursors were introduced into the hydrophobic cavity of the cage, followed by in situ reduction with $NaBH_4$ to generate Pd NCs encapsulated within the internal cavity. This approach yielded monodisperse nanoclusters (caged Pd NCs, termed PR) with an average diameter of 0.77 ± 0.23 nm (Figure 1b–c). High-resolution transmission electron microscopy (HR-TEM) characterization (Figure S1) further confirms the presence of Pd NCs. Elemental mapping analysis demonstrates that the obtained ultra-fine Pd NCs are highly distributed within the cage material (Figure S2). The successful synthesis of cage RCC3 was confirmed by NMR spectroscopy (see details in experimental section and characterization in Figure S3–S6, supporting information), and the similar spectral features after Pd reduction confirmed the structural integrity of the host framework (Figure S7). Cage CC3 was selected owing

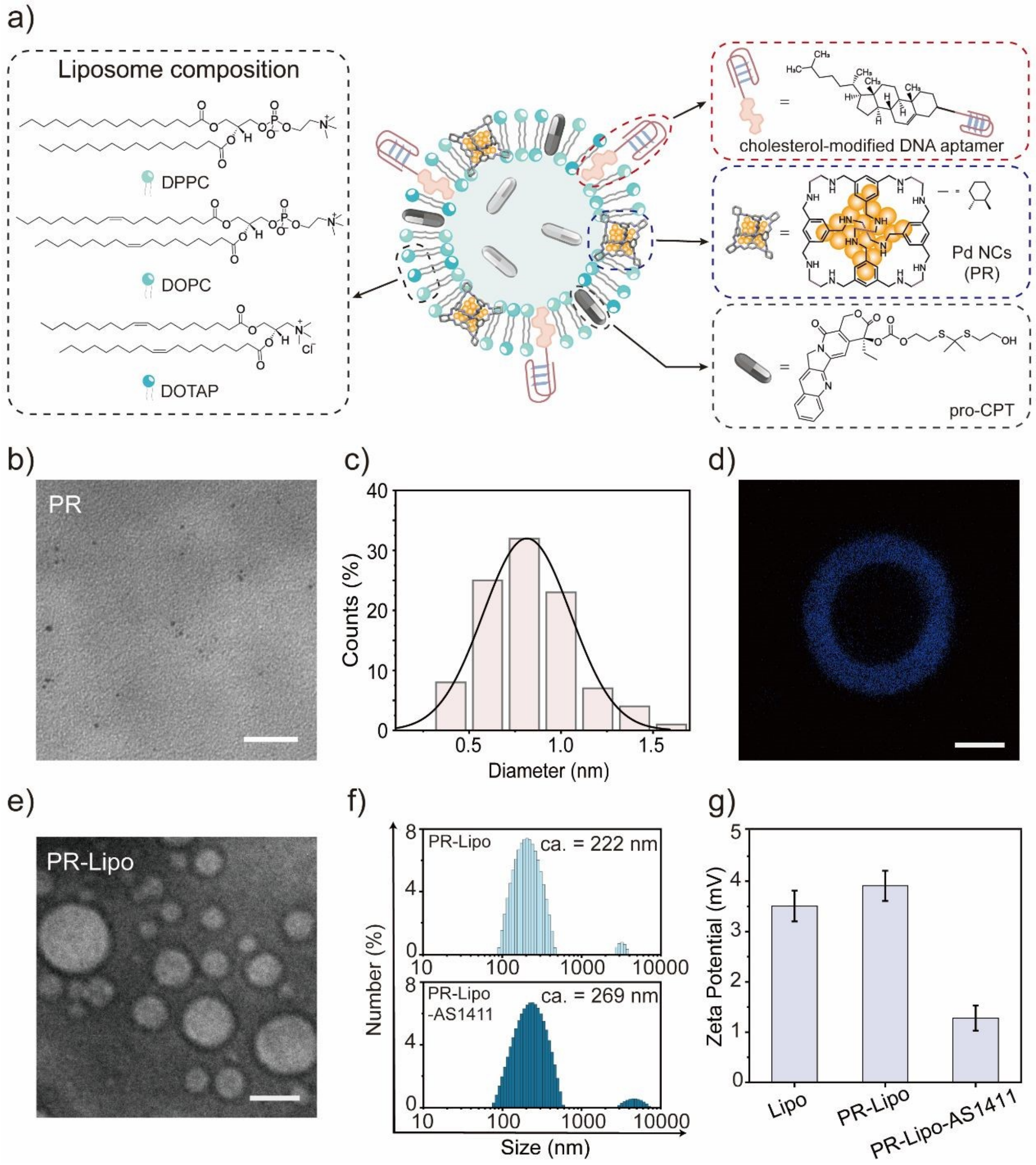

Figure 1 Design and characterization of the liposome delivery system. a) Schematic illustration of the formulation of the multifunctional liposome. b) TEM image of PR nanoclusters encapsulated with molecular cage RCC3 (termed PR); scale bar: 20 nm. c) Size distribution of PR shown in Figure 1b. d) Confocal laser scanning microscopy (CLSM) image of liposomes labelled with fluorescent molecular cages, excitation 405 nm. Blue circles indicate the presence of molecular cages in the lipid bilayer; scale bar: 100 μm. e) TEM image of PR-loaded liposomes (termed PR-Lipo); scale bar: 50 nm. f) DLS measurements of liposomes. g) Zeta potential measurements of three different liposomes: blank liposome (Lipo), PR-Lipo and PR-loaded liposomes modified with AS1411 (PR-Lipo-AS1411). Data were presented as mean ± S.D. (n = 3).

View Article Online
DOI: 10.1039/D6SC02576E

to its high solubility, robust stability, and intrinsic hydrophobicity, which ensure molecular-level dispersion in solution and efficient encapsulation of metal precursors. In addition, the X-ray photoelectron spectroscopy (XPS) spectra (Figure S8) demonstrate characteristic peaks at binding energies of 335.2 eV and 340.5 eV, corresponding to metallic Pd^0. An additional set of peaks at 336.8 eV and 342.1 eV was also observed, corresponding to Pd^{2+}. These results indicate that both Pd^0 and Pd^{2+} species exist, which is consistent with the commonly reported form of Pd element in Pd-based nanozymes[20,44]. N_2 adsorption–desorption experiments were also performed (Figure S9). The desolvated empty cage RCC3 exhibits almost no N_2 uptake due to structural flexibility, leading to pore collapse. In contrast, after palladium loading, PR displays enhanced microporous adsorption characteristics. This observation is consistent with previous literatures[15]. The reduced imine bonds in RCC3 cage increase its framework flexibility, making it prone to structural collapse upon desolvation. Notably, the confined growth of Pd NCs within the cage cavities acts as a "molecular template" that reopens the collapsed framework and restores pore accessibility. Therefore, the porosity of PR does not arise solely from the empty cage but rather from a "cluster–cage" synergistic stabilization. Infrared spectroscopy (IR) and thermogravimetric analysis (TGA) were conducted to comprehensively evaluate thermal stability and composition. The IR spectrum of PR is nearly identical to that of the pristine RCC3 cage (Figure S10). All characteristic peaks are well preserved. The signals at 3300 cm^{-1} and 1114 cm^{-1} correspond to $–NH_2$ and C–N vibrations, respectively. The peaks at 2926 cm^{-1} and 2852 cm^{-1} are attributed to $–CH_2–$ stretching; and the signals at 1603 cm^{-1} and 1448 cm^{-1} indicate the presence of –C=C– bonding. Moreover, TGA results demonstrate that both RCC3 and PR exhibit good thermal stability under a nitrogen atmosphere below 200 °C（Figure S11). Negligible weight loss was observed in this temperature range, indicating that the framework structure remains intact after palladium encapsulation. These results provide strong evidence that the encapsulation of Pd NCs does not disrupt the structure of the RCC3 molecular cage.

To construct a suitable vehicle capable of transporting these caged Pd NCs to the plasma membrane with spatiotemporal precision, we drew inspiration from how extracellular vesicles fuse with target cells and insert their lipids into the cytoplasmic membrane. Based on this principle, we engineered a membrane-fusogenic liposomal platform using a thin-film hydration-extrusion method (Figure 1a and Figure S12). Considering the

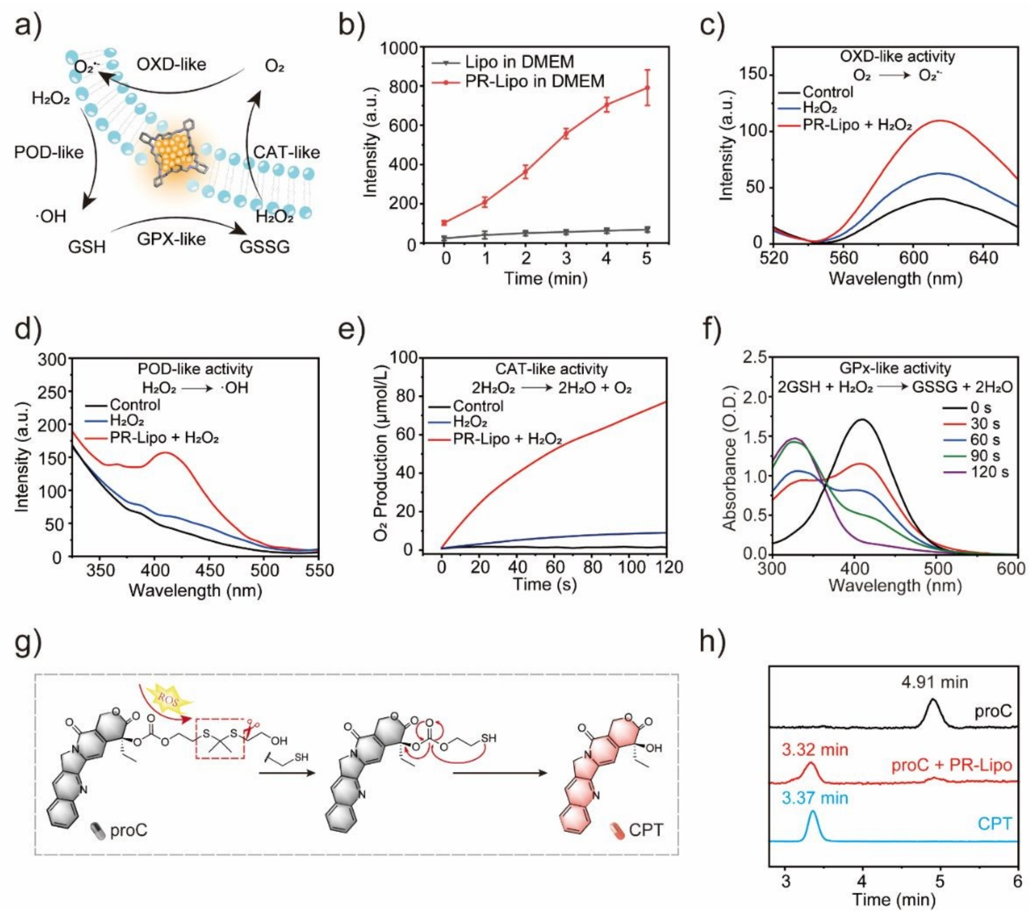

Figure 2 Enzyme-like activities of PR-Lipo and ROS-mediated prodrug activation. a) Enzyme-mimicking activities of PR-Lipo. b) Time-dependent fluorescence changes of 2′,7′-dichlorodihydrofluorescein in DMEM, in the presence of PR-Lipo and H_2O_2. c) OXD-like activity: fluorescence spectra of DHE (20 μM) under different conditions. d) POD-like activity: fluorescence spectra of TA (20 μM) under different conditions. e) CAT-like activity: time-dependent O_2 generation. f) GPx-like activity: GSH consumption at different time intervals, characterized via probe DTNB. g) ROS-activated CPT release from the prodrug proC. h) HPLC analysis of ROS-mediated prodrug activation in the presence of PR-Lipo and H_2O_2. Data were presented as mean ± S.D. (n = 3). PR-Lipo: 20 μg·mL⁻¹, H_2O_2 :100 mM.

View Article Online
DOI: 10.1039/D6SC02576E

native composition of cell membranes, liposomes were prepared using 1,2-dioleoyl-sn-glycero-3-phosphocholine (DOPC), 1,2-dipalmitoyl-sn-glycero-3-phosphocholine (DPPC), and the cationic lipid 1,2-dioleoyl-3-trimethylammonium-propane (DOTAP) in a molar ratio of 1:1:0.2. Zwitterionic DPPC and DOPC impart high biocompatibility with endogenous phosphatidylcholines, while DOTAP, being positively charged, enhances electrostatic interactions with the negatively charged cellular membrane, thereby facilitating membrane fusion. Cholesterol-modified DNA was incorporated as a targeting ligand to further promote selective fusion with the desired cell population. Maintaining the initial lipid ratio, we first examined whether the hydrophobic molecular cage could indeed embed within the liposomal bilayer. Given its hydrophobic surface, we hypothesized that the cage would partition into the bilayer through hydrophobic interactions, thereby enabling Pd NCs encapsulated inside the cage to be co-embedded in the membrane. By using a fluorescent cage CC19 (Figure S13–14, structurally analogous to cage RCC3), bright fluorescence outlines the liposomal membrane under confocal microscopy (termed CC19-Lipo, Figure 1d), demonstrating successful incorporation of the hydrophobic cages without disrupting bilayer morphology. The liposomes remained uniform and spherical, indicating that cage insertion does not perturb membrane assembly. These findings suggest that Pd NCs encapsulated within cages should likewise be incorporated within the lipid bilayer. According to published literature, the organic molecular cage RCC3 possesses the ability to anchor into phospholipid bilayers[45]. Furthermore, PR prepared using RCC3 as a template were also confirmed by cryo-TEM to be localized on the phospholipid bilayer[45]. Therefore, it can be inferred that PR has the inherent capability to embed into liposomal membranes. Transmission electron microscopy (TEM) revealed well-defined spherical morphology of liposomes incorporated with Pd NCs (termed PR-Lipo, Figure 1e). Dynamic light scattering (DLS) measurements showed no significant changes in hydrodynamic diameter and zeta potential after PR incorporation (Figure 1f–g and Figure S15a–S16). Their size in culture medium containing 10% FBS over 24 hours further confirms the structural stability of the PR-Lipo (Figure S15b). Inductively coupled plasma (ICP) analysis quantifies the Pd content at approximately 0.26% (Table S2). These results demonstrate the successful construction of a membrane-fusogenic liposomal system with excellent colloidal stability and integrated ultrasmall Pd NCs. Zeta potential measurements showed a clear decrease after incorporation of cholesterol-modified DNA, indicating the successful incorporation of negatively charged DNA strands (termed PR-Lipo-AS1411, Figure 1g).

The molecular cage, featuring a porous framework with open windows, directs the formation of ultrasmall caged Pd NCs and exposes accessible catalytic sites, which exhibited excellent catalytic performance and multiple enzyme-mimicking features, including peroxidase (POD)-, catalase (CAT)-, oxidase (OXD)-, and glutathione peroxidase (GPx)-like activities (Figure 2a).[14] Specifically, the CAT-like activity decomposes H_2O_2 into O_2 and H_2O. This activity is crucial for converting the high concentration of H_2O_2 in the tumor microenvironment into O_2, which serves as the primary source for subsequent reactive oxygen species (ROS) generation. The generated O_2 is then converted into superoxide anion radicals ($O_2^{\bullet-}$) via the OXD-like activity of Pd. Meanwhile, the POD-like activity of Pd catalyzes the conversion of H_2O_2 into hydroxyl radicals (•OH)[20, 46]. Thus, the multiple enzyme-mimicking activities of PR (CAT, OXD, POD, GPx) operate synergistically in a cascade manner. CAT-like activity supplies O_2, which is subsequently activated to $O_2^{\bullet-}$ via OXD-like activity. POD-like activity contributes •OH and GPx-like activity promotes ROS accumulation by depleting GSH. Therefore, these multiple enzyme-like activities work in concert to enhance ROS accumulation. We systematically evaluated the catalytic behavior and ROS-generating capability of PR-Lipo in cell culture medium. Using the 2′,7′-dichlorodihydrofluorescein (DCFH) probe, the ROS-generating capability of PR-Lipo in Dulbecco's Modified Eagle Medium (DMEM) was examined, in the presence of H_2O_2. An increase in probe fluorescence was observed, indicating continuously produced ROS over time (Figure 2b and Figure S17). ROS generation tests were also performed *in vitro* under a high H_2O_2 concentration (100 μM) that mimics the tumor microenvironment. As shown in the Figure S18, in the presence of both PR and H_2O_2, the addition of the DCFH probe revealed a time-dependent increase in fluorescence intensity, and the reaction rate was significantly higher than that observed under the control condition with 100 μM H_2O_2 alone.

The OXD-like activity of PR-Lipo was probed using dihydroethidium (DHE), a specific $O_2^{\bullet-}$ indicator. Upon addition of PR-Lipo and H_2O_2, a pronounced enhancement of the emission at 610 nm was observed in the Pd-containing system, confirming the generation of $O_2^{\bullet-}$ (Figure 2c). Similarly, •OH production was detected using terephthalic acid (TA) as a specific fluorogenic probe, where PR-Lipo + H_2O_2 system yielded a strong increase in the 425 nm emission band as compared to control groups (Figure 2d). The CAT-like activity of PR-Lipo was further verified by monitoring dissolved O_2 in H_2O_2 solutions (Figure 2e), demonstrating that PR-Lipo effectively decomposes H_2O_2 for local oxygenation, which is expected to relieve local hypoxia and, meanwhile, supply reactants for ROS generation. To evaluate the GPx-like activity of PR-Lipo, we quantified glutathione (GSH) consumption by monitoring the conversion of 5,5'-dithiobis(2-nitrobenzoic acid) (DTNB, Ellman's reagent) into yellow 2-nitro-5-thiobenzoic acid (TNB). In the presence of PR-Lipo, GSH was rapidly depleted, as evidenced by a pronounced time-dependent decrease in the absorbance of TNB at 412 nm (Figure 2f). To distinguish between GPx-like activity and nonspecific GSH depletion induced by oxidative stress, we designed and performed control experiments (Figure S19). Specifically, we added ROS scavengers to the reaction system, including dimethyl sulfoxide (DMSO, a •OH scavenger) and superoxide dismutase (SOD, an antioxidant enzyme that scavenges $O_2^{\bullet-}$). By adding these scavengers, we aimed to inhibit nonspecific oxidation and evaluate whether the material itself retains the ability to catalyze GSH. The experimental results showed that after the addition of DMSO and SOD to reduce ROS levels in the system, the rate of GSH depletion indeed decreased significantly. This finding confirms that a portion of GSH consumption is indeed caused by ROS-mediated oxidation. However, even after the addition of scavengers, sustained GSH conversion was still observed. This indicates that our material possesses intrinsic GPx-like activity, and nonspecific oxidative depletion cannot be ruled out as a contributing factor to GSH depletion in our system.

Furthermore, additional control experiments were performed. Regarding the liposome-only control (Figure 2b), after the addition of DCFH probe to liposomes alone, almost no changes were observed in fluorescence signal, indicating that liposomes themselves do not possess ROS-generating capability. Moreover, RCC3 alone (without Pd loading) didn't generate ROS, as shown in Figure S20. The results demonstrate that the catalytic activity is attributed to the loaded Pd NCs. In the heat-inactivated catalyst system, PR retains high catalytic activity even at 100 °C[47]. The ROS generation capability of the catalyst

View Article Online
DOI: 10.1039/D6SC02570E

after heat treatment at 100 °C using the DCFH probe was assessed. As shown in Figure S21, the catalytic activity remained almost unaffected. Larger Pd nanoparticles (cPd NPs) were also synthesized as a control[48]. Under identical experimental conditions, we systematically compared the ROS generation kinetics of PR (~0.77 nm) and cPd NPs (~9 nm). Using a ROS probe DCFH to monitor catalytic activity, the results clearly showed that the ROS generation rate of cPd NPs was significantly lower than that of the PR system (Figure S22). Thus, the ROS-generating capability of Pd is indeed strongly dependent on particle size. Consistent with our observations, it has been reported that the enzyme-mimetic catalytic activity of noble metal nanocrystals increases progressively with decreasing particle size[49]. Furthermore, the POD-like activity of metal nanoparticles exhibits size dependence, with sub-nanometer clusters (< 2 nm) demonstrating superior catalytic efficiency[50]. In our study, PR exhibits an ultrasmall size, high specific surface area, and cage-like porous structure that provides abundant accessible active sites, which account for its high catalytic activity, and similar phenomenon was also observed in other studies[15]. To further evaluate catalytic stability, we conducted X-ray diffractometer (XRD) characterization of the PR catalyst

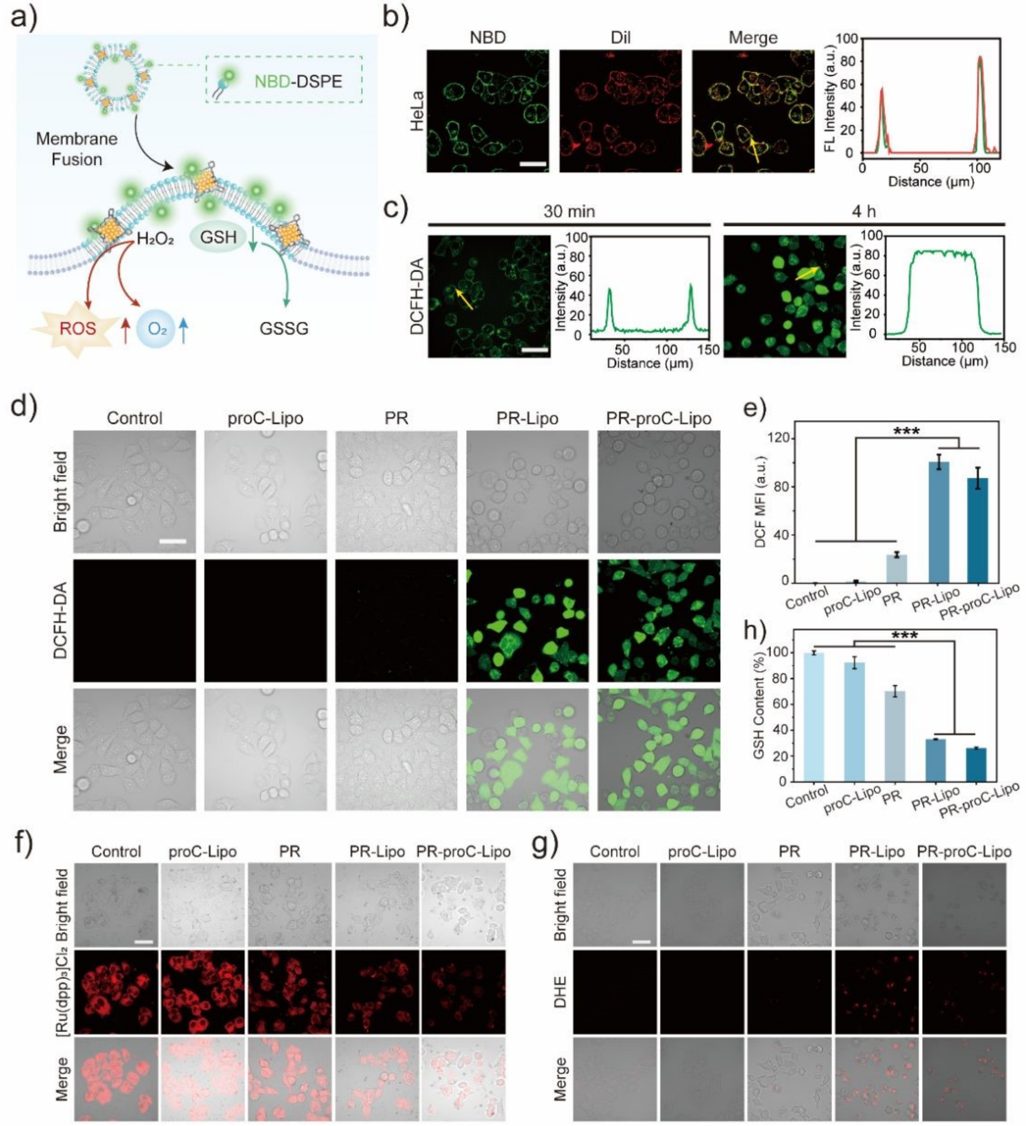

Figure 3. Membrane fusion-induced oxidative effects. a) Schematic illustration of the NBD-DSPE labeled PR-Lipo interacting with the cell membrane and exhibiting the enzyme-like catalytic behavior. b) CLSM images (left) and corresponding fluorescence intensity profiles (right) showing the co-localization of NBD-DSPE (green) with DiI (red) in HeLa cells treated with NBD-DSPE labeled PR-Lipo. Scale bars: 100 μm. c) CLSM images (left) and corresponding fluorescence intensity profiles (right) showing the time-dependent ROS generation in HeLa cells after treatment with PR-Lipo. Scale bars: 100 μm. d) CLSM images of ROS (green fluorescence) detected by DCFH-DA in cells under normal culture conditions and after treatment with proC-Lipo, PR, PR-Lipo and PR-proC-Lipo, respectively. Scale bars: 100 μm. e) Quantitative analysis of DCF in HeLa cells after different treatments. f) CLSM images of intracellular O_2 levels detected by $[Ru(dpp)_3]^{2+}Cl_2$ in HeLa cells with different treatments. Scale bars: 100 μm. g) CLSM images of intracellular $O_2^{\bullet-}$ production in HeLa cells with different treatments using DHE as the $O_2^{\bullet-}$ fluorescence indicators. Scale bars: 100 μm. h) Intracellular GSH level in HeLa cells after different treatments. Data were presented as mean ± S.D. (n = 3). (*p < 0.05, **p < 0.01, ***p < 0.001).

View Article Online
DOI: 10.1039/D6SC02576E

before and after reaction in the presence of the physiologically relevant nucleophile glutathione (GSH). As shown in Figure S23, no significant changes in the characteristic diffraction peaks were observed before and after the reaction, indicating that the catalyst possesses good stability under these conditions.

Given the potent ROS-generating properties of Pd NCs, we hypothesized that Pd-induced ROS could be used to activate ROS-responsive prodrugs (Figure 2g). To test this concept, a ROS-responsive prodrug was designed and synthesized, termed proC (synthetic route shown in Figure S24–25). Successful encapsulation of proC into liposomes was confirmed by UV absorbance at 350 nm, with an encapsulation efficiency of ~87.5% (Figure S26). The ROS-cleavable thioketal linker (TK) in proC was readily cleaved, releasing the active drug camptothecin (CPT). HPLC analysis confirmed the cleavage of the TK linker, in the presence of PR-Lipo and H_2O_2, proC was almost completely converted to CPT within 5 h (Figure 2h and Figure S27). Besides, we compare the extent of prodrug cleavage in the presence of H_2O_2 alone versus H_2O_2 + PR-Lipo (Figure S28). The experimental results showed that H_2O_2 alone does induce partial conversion of the prodrug to CPT. However, the conversion efficiency was lower than that observed in the presence of both PR-Lipo and H_2O_2. These findings indicate that while direct H_2O_2-induced cleavage of the thioketal linker does occur to some extent, the presence of PR-Lipo effectively accelerates and enhances the release of the active drug CPT.

The fusion capability of the liposomes with cells was then evaluated at the cellular level. Liposomes were labeled with a fluorophore-modified lipid (NBD-DSPE) and co-incubated with HeLa cells for 15 min. Distinct liposomal fluorescence was observed at the membrane and exhibited strong colocalization with the red fluorescence of the membrane dye DiI, yielding a yellow signal on the plasma membrane (Figure 3a–b). The fusion process probably mediates immobilization of PR at the membrane interface. The liposome formulation used in this study has been widely employed for cell-membrane-targeted delivery[41, 43, 51], with membrane localization lasting up to 48 hours, and is thus considered a reliable membrane-fusogenic liposome for plasma membrane targeting. The key component promoting cell membrane targeting is the inclusion of a certain amount (5%) of DOTAP, whose positive charge significantly enhances the retention of liposomes on the cell membrane surface[51]. To further validate that this system effectively enables membrane delivery of molecular cages, we employed a fluorescent molecular cage (PTC) as a probe and compared delivery using liposomes with or without DOTAP (See detailed characterizations of PTC in supporting information, Figure S29). As shown in Figure S30, in the absence of DOTAP, fluorescence was observed in the cytoplasm rather than on the cell membrane. In contrast, delivery with DOTAP-containing liposomes resulted in fluorescence localized on the cell membrane, indicating successful membrane-targeted delivery. To further investigate the delivery mechanism of our liposome, we adopted the strategy of pretreating cells with inhibitors[52]. A series of classical endocytosis inhibitors targeting clathrin-mediated, caveolin-mediated, and macropinocytic pathways were introduced. As shown in Figure S31, pretreatment with chlorpromazine (CPZ, a clathrin-dependent endocytosis inhibitor), methyl-β-cyclodextrin (M-β-CD, a caveolin inhibitor), or ethylisopropylamiloride (EIPA, a macropinocytosis inhibitor) had negligible effects on the membrane-targeted delivery of PR-Lipo. Fluorescently labeled liposomes remained clearly visible at the cell periphery with colocalization with the plasma membrane. These results confirm that PR-Lipo enter cells through membrane fusion. Regarding the effect of particle size on membrane anchoring efficiency, the diameter of PR is smaller than the thickness of the cell membrane phospholipid bilayer (ca. 5 nm). Importantly, the hydrophobic nature of the RCC3 cage enables favorable interactions with the lipid chains. We therefore propose that this combined attribute of sub-bilayer-thickness dimensions and hydrophobicity is a key determinant for stable membrane anchoring. In contrast, particles larger than the bilayer thickness would likely encounter substantial steric hindrance, compromising their insertion and stable retention. This size-dependent anchoring behavior is consistent with a previous study[45], demonstrating that molecular cages can achieve stable membrane insertion when their dimensions are compatible with the bilayer thickness (ca. 5 nm). Thus, we infer that hydrophobic nanoparticles with a diameter less than the bilayer thickness are capable of anchoring within the lipid membrane, provided they possess appropriate surface chemistry.

As multi-enzyme-mimicking activities of PR effectively promote ROS generation under physiological concentrations of H_2O_2 levels, we employed the oxidant-sensitive probe 2′,7′-dichlorodihydrofluorescein diacetate (DCFH-DA) to monitor ROS generation in cells by confocal microscopy (Figure 3c). Green fluorescence from the oxidized product dichlorofluorescein (DCF) was first detected at the cell membrane within 30 min, indicating local ROS generation at the plasma membrane. Then the fluorescence gradually diffused into the cytosol at 4 h. We systematically investigated ROS accumulation among different groups. Upon incubation with PR-Lipo or PR-proC-Lipo, HeLa cells exhibited pronounced oxidative stress, as evidenced by strong green fluorescence (Figure 3d–e). In contrast, fluorescence was not observed in cells treated with proC-Lipo alone, indicating negligible ROS generation. Notably, cells treated with PR-proC-Lipo displayed lower fluorescence intensity than those treated with PR-Lipo alone, likely due to consumption of ROS during the activation of the proC prodrug. Strikingly, cells treated with an equivalent amount of free PR showed almost no detectable green fluorescence (Figure 3e). These results indicate that the liposome-mediated membrane-anchored system enables PR to generate substantially more ROS. Notably, the liposome formulation used in this study contains DOTAP, whose positive charge significantly promotes liposome fusion with the cell membrane[51]. Therefore, we further included a control group using liposomes without DOTAP (which enter cells primarily via endocytosis) and compared it with the DOTAP-containing liposome group (membrane-anchored group). Under identical Pd concentrations and treatment conditions, we compared ROS generation capacity between these two delivery routes. Given that these experiments were conducted in living cells, the influence of complex physiological environmental factors was inherently taken into account. As shown in Figure S32, the green fluorescence signal observed in the PR-Lipo (with DOTAP) was significantly stronger than that of the control group in the absence of DOTAP. These results demonstrate that Pd catalysts localized on the cell membrane generate more ROS, exhibiting stronger catalytic performance. These observations further support that membrane anchoring localizes PR within a relatively clean microenvironment and substantially preserves its catalytic activity from deactivation by abundant nucleophiles, proteins, and amino acids in cytosolic environment.[26]

Since PR exhibits CAT-like activity and can decompose H_2O_2 into H_2O and O_2, we investigated whether our system could modulate tumor-associated hypoxia. Using the oxygen-sensitive probe $[Ru(dpp)_3]Cl_2$ (Figure 3f), cytosolic oxygen levels was

View Article Online
DOI: 10.1039/D6SC02576E

imaged. Under normoxic conditions, the [Ru(dpp)$_3$]Cl$_2$ probe shows negligible fluorescence, whereas under hypoxia, the probe emits strong red fluorescence. PR-Lipo or PR-proC-Lipo treatment markedly alleviated cellular hypoxia, as indicated by the significant decrease in red fluorescence within the cytosol. This effect is attributed to Pd-mediated catalytic decomposition of H_2O_2 into O_2. Intracellular $O_2^{\bullet-}$ generation was further examined using DHE probe, which produced distinct red fluorescence (Figure 3g). Consistent with the DCF results, PR-Lipo induced strong $O_2^{\bullet-}$ accumulation, while PR-proC-Lipo resulted in a relatively lower fluorescence intensity, and free PR again produced almost no detectable signal, corroborating the conclusions above. The elevated intracellular oxygen not only enhances the catalytic production of $O_2^{\bullet-}$ but may also contribute positively to suppressing tumor metastasis. In addition, both PR-Lipo and PR-proC-Lipo-treated cells showed significant decrease in GSH levels (Figure 3h and Figure S33). This reduction can be attributed to GPx-like activity of PR.

Having confirmed enzyme-mimicking activities and ROS generation at the cellular level, the ROS-induced cytotoxic effects of membrane-anchored Pd and endocytosed PR (caged Pd NCs) were systematically evaluated (Figure 4a). Both systems displayed dose-dependent effects on cell viability. At an identical Pd concentration (2 μg/mL), membrane-anchored Pd reduced cell viability to ~20%, whereas cells treated with endocytosed PR retained nearly 80% viability. A comparable decrease in viability (<20%) was observed for endocytosed PR only when the dosage exceeded 10 μg/mL. These results suggest that freely internalized PR generates ROS inefficiently, likely due to deactivation by cytosolic components, whereas membrane confinement preserves catalytic activity and enhances ROS-induced oxidative efficacy. Then, the cell viability was evaluated for PR-Lipo and PR-proC-Lipo. Both systems also exhibited dose-dependent effects toward HeLa and 4T1 cells (Figure S34). PR-Lipo exhibited concentration-dependent viability toward HeLa cells, while the co-delivery system comprising PR and the prodrug proC (termed PR-proC-Lipo) demonstrated decreased viability compared with PR-Lipo alone. Based on the CCK-8 cell viability data, we fitted dose–response curves for free PR and PR-Lipo (Figure S35). Nonlinear regression analysis was performed to calculate the half-maximal inhibitory concentrations (IC50). For free PR, the IC50 value was determined to be 5.2 μg/mL. In contrast, PR-Lipo exhibited significantly enhanced cytotoxicity, with an IC50 value of 1.3 μg/mL. Thus, PR-Lipo is approximately four times more potent than free PR on the tested cell line. To assess the intrinsic safety of the prodrug, we further examined the dose-dependent cytotoxicity of proC and its active parent drug CPT in HeLa cells (Figure S36). CPT induced a steep decline in cell viability with increasing concentration, whereas proC exhibited substantially lower toxicity at equivalent does. This difference highlights the biocompatibility of the prodrug prior to ROS-mediated activation.

Live/dead cell staining experiments further visualized the efficient cytotoxic activity (Figure 4b). Flow cytometry analysis using Annexin V-FITC/PI revealed significant cell death in HeLa cells after incubation with PR-proC-Lipo compared with other control groups (Figure 4c). Notably, cells treated with an equivalent amount of caged Pd NCs in absence of liposomes largely remained viable, indicating that free PR failed to generate

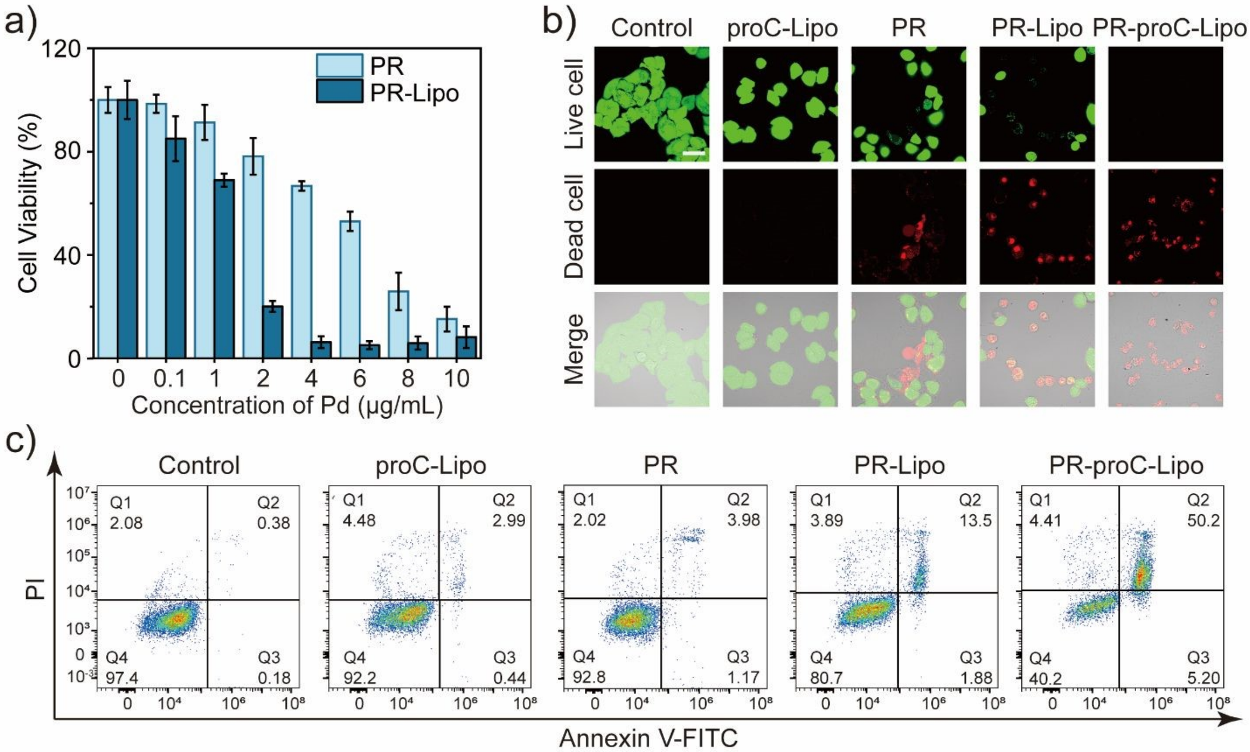

Figure 4. Cellular cytotoxic efficacy of the liposome delivery system. a) Cytotoxicities of PR-Lipo and PR at varied concentrations against HeLa cells by CCK8 assay. b) CLSM images of HeLa cells after different treatments. Cells were treated with normal culture, proC-Lipo, PR, PR-Lipo and PR-proC-Lipo, respectively. Viable cells were stained with calcein AM (green fluorescence); dead cells were stained with propidium iodide (PI, red fluorescence). Scale bars: 100 μm. c) Flow cytometry analysis of cell apoptosis using Annexin V-FITC and PI staining after treatment with normal culture, proC-Lipo, PR, PR-Lipo and PR-proC-Lipo. Data were presented as mean ± S.D. (n = 3).

View Article Online
DOI: 10.1039/D6SC02576E

ROS efficiently due to the lack of membrane confinement, in agreement with the results shown in Figure 3d. In contrast, membrane-anchored PR retained its catalytic activity and efficiently promoted ROS accumulation, demonstrating that anchoring PR within the relatively clean membrane interface effectively preserves its catalytic function. Taken together, these findings establish that membrane-anchored PR efficiently promotes prodrug activation and cell killing, offering a promising strategy for targeted cancer therapy.

Given the high binding affinity of the AS1411 aptamer toward nucleolin overexpressed on tumor cell surfaces, AS1411-functionalized liposomes were designed to enable selective tumor targeting and controlled membrane delivery (Figure S37a). To visualize aptamer-mediated targeting, the AS1411 aptamer was labeled with dye Cyanine5 (Cy5). Obvious red fluorescence of Cy5 was observed at the membrane of human prostate cancer cell line DU145, murine mammary carcinoma cell line 4T1 and HeLa cells, exhibiting strong colocalization with the green fluorescence of the membrane dye DiO (Figure S37b). In contrast, negligible red fluorescence was detected on normal HUVEC cells (human umbilical vein endothelial cells), demonstrating the tumor-selective targeting ability of AS1411-functionalized liposomes and highlight their potential for antitumor therapy. In addition, control experiments were performed using 293T cells (human embryonic kidney cells),

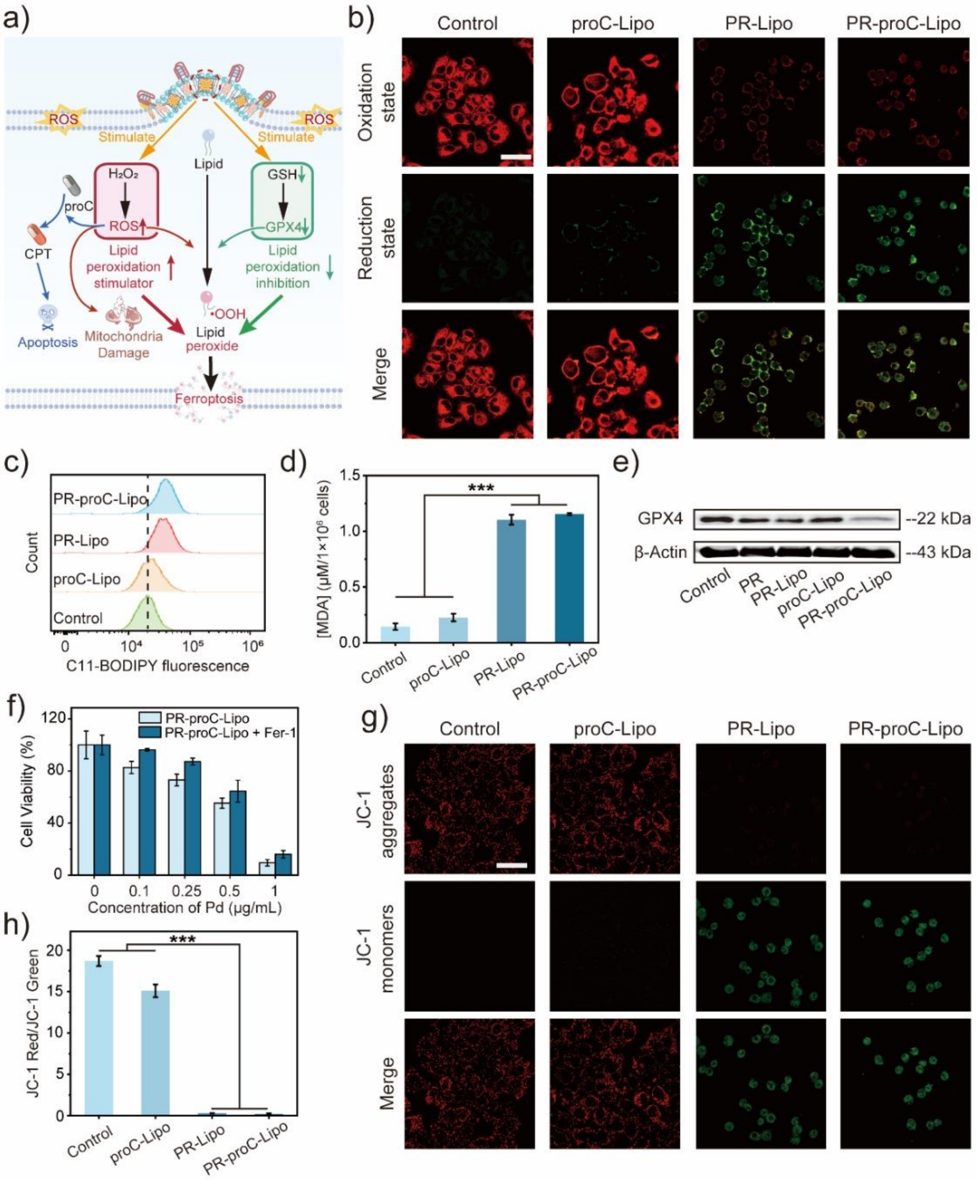

Figure 5 *In vitro* mechanism underlying the cytotoxic effect of PR-proC-Lipo. a) The membrane fusion of PR-proC-Lipo produces ROS to activate the prodrug, inducing ferroptosis and apoptosis. CLSM images (b) and flow cytometry analysis (c) of intracellular lipid peroxide (LPO) levels detected with C11-BODIPY 581/591 in HeLa cells treated with normal culture, proC-Lipo, PR-Lipo and PR-proC-Lipo, respectively. Scale bars: 100 μm. d) Intracellular MDA levels in HeLa cells after different treatments. e) Western blot analysis of GPX4 expression in cells subjected to different treatments. f) Viability of HeLa cells after treatment with PR-proC-Lipo at varying concentrations in the presence or absence of ferroptosis inhibitor (Fer-1). CLSM images (g) and MFI ratio of JC-1 aggregates (red) and JC-1 monomer (green) (h) illustrating changes in mitochondrial membrane potential (MMP) in HeLa cells treated with normal culture, proC-Lipo, PR-Lipo and PR-proC-Lipo, respectively. Scale bars: 100 μm. Data were presented as mean ± S.D. (n = 3). (*p < 0.05, **p < 0.01, ***p < 0.001).

View Article Online
DOI: 10.1039/D6SC02576E

which are widely used as a non-malignant control model in biomedical research, particularly in studies on ferroptosis and cancer-selective therapy[53-56]. As shown in Figure S38, AS1411-functionalized liposomes exhibited minimal membrane fusion with 293T cells, further supporting the selective cancer-targeting capability of the AS1411-mediated delivery system.

As PR was anchored on the phospholipid-rich membrane, it is highly possible that localized Pd-induced ROS generation could directly cause oxidative damage on the plasma membrane, triggering lipid peroxidation (LPO), Figure 5a. Intracellular LPO levels were assessed using the lipid-peroxidation-sensitive probe BODIPY-C11. Both confocal microscopy and flow cytometry revealed that cells treated with PR-Lipo and PR-proC-Lipo exhibited intense green fluorescence (Figure 5b–c and Figure S39), indicating substantial accumulation of lipid peroxides.

The LPO was further verified by elevated intracellular MDA levels, a typical byproduct of LPO. Cells treated with PR-Lipo and PR-proC-Lipo exhibited significantly higher MDA levels than those in other control groups, providing additional evidence of LPO (Figure 5d and Figure S40–S41). As GPX4 is a key enzyme for defending against LPO and a ferroptosis-associated key characteristic, its expression was further evaluated by Western blotting. Treatment with PR-proC-Lipo and PR-Lipo led to down-regulation of GPX4 expression, suggesting that Pd-induced excessive lipid peroxidation depleted the enzyme (Figure 5e and Figure S42). Notably, treatment with PR alone slightly reduced GPX4 expression, underscoring the crucial role of membrane anchoring for maintaining Pd activity. Given that intracellular ROS accumulation and LPO are critical hallmarks of ferroptosis, cells were co-treated with ferrostatin-1 (Fer-1), a specific ferroptosis inhibitor. Fer-1 partially suppressed PR-proC-Lipo-induced cell death, confirming that ferroptotic pathways contributed to the observed cytotoxicity (Figure 5f). In addition, ferroptosis is often accompanied by severe mitochondrial dysfunction. To evaluate mitochondrial status under oxidative stress, we monitored mitochondrial membrane potential (MMP) using JC-1 staining. In healthy mitochondria, JC-1 aggregates emit red fluorescence (JC-1/A), whereas in damaged mitochondria, JC-1 exists as monomers emitting green fluorescence (JC-1/M). Both PR-Lipo and PR-proC-Lipo treatment caused a substantial increase in green fluorescence, indicating stronger MMP depolarization (Figure 5g–h and Figure S43–S44). The above results demonstrated that membrane-anchoring Pd system enables *in situ* ROS generation and effectively activates LPO.

Encouraged by its promising *in vitro* performance, the *in vivo* antitumor efficacy of the system was evaluated on 4T1 tumor-bearing BALB/c mice. To investigate the *in vivo* biodistribution and tumor enrichment, dye Cy5-labeled liposome samples with identical lipid composition (PR-Lipo-AS1411-Cy5) were used. The results showed that fluorescence signals accumulated at the tumor site within 2 h post-injection. The

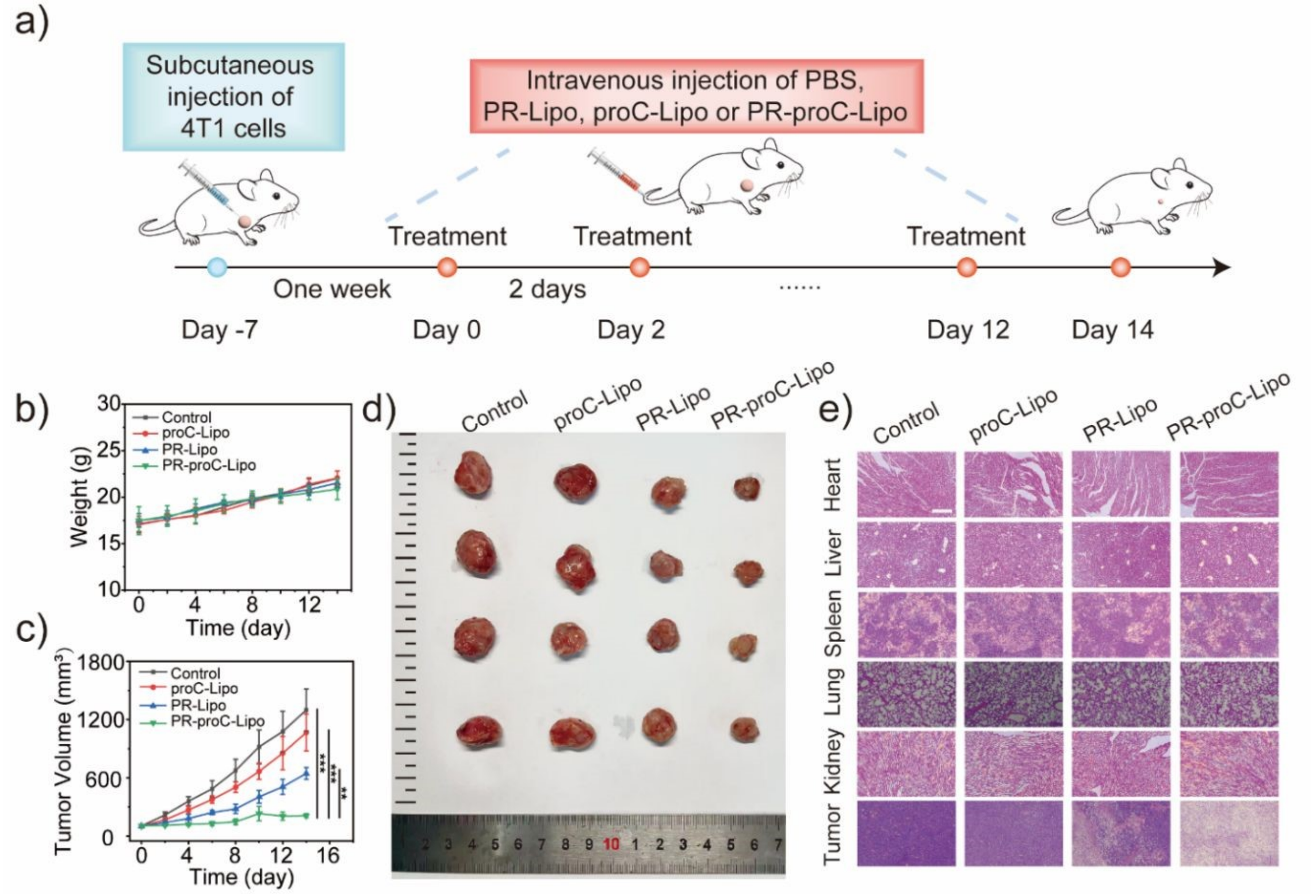

Figure 6 *In vivo* therapeutic analysis. a) Schematic illustration of mice model and treatment schedule. The tumor volume and weight were measured every 2 days during the treatment. b) Changes of body weights after the indicated treatments. c) Changes of tumor volume after the indicated treatments. d) Images of the excised tumors on day 14 after different treatments. e) H&E staining of tumor tissues after 14 days of treatment. Scale bar: 100 μm. Data were presented as mean ± S.D. (n = 4). (*p < 0.05, **p < 0.01, ***p < 0.001).

fluorescence reached maximum at 4 h and maintained retention for up to 24 h (Figure S45a–b). The dissected organs and tumor were collected for *ex vivo* imaging after mice were sacrificed at 4 h post injection. PR-Lipo-AS1411-Cy5 exhibited distinct fluorescence in the tumor tissue (Figure S45c). In addition, the biodistribution of Pd in tumors and other organs after intravenous administration was evaluated by ICP-MS, showing that Pd-Lipo was rapidly accumulated in tumors 4 h after injection (Figure S46). This confirms that AS1411-functionalized liposomes effectively enhance tumor targeting and retention, providing a basis for subsequent therapeutic evaluation. The *in vivo* therapeutic effects were further investigated in tumor-bearing mice, which were randomly divided into four groups (groups 1-4: treated with PBS, proC-Lipo, PR-Lipo, and PR-proC-Lipo, respectively, n = 4 per group). Treatments were administered via tail-vein injection on day 0, and tumor growth and body weight were monitored over 14 days (Figure 6a). No significant body weight changes were observed during treatment (Figure 6b), indicating good biocompatibility and no systemic toxicity. The tumor size was measured every 2 days during the treatment and the relative growth curve was recorded (Figure 6c). The tumor volumes in control groups showed significant increase during the period, while the group treated with PR-proC-Lipo showed a pronounced suppression effect on the tumor growth.

After treatment, excised tumors were photographed and histological analysis were performed. Consistent with tumor growth curves, it revealed that proC-Lipo alone showed negligible tumor inhibition, PR-Lipo exhibited moderate suppression, and PR-proC-Lipo combination treatment led to the most pronounced tumor reduction (Figure 6d). Histochemical analysis by H&E staining demonstrate severe damage in PR-proC-Lipo-treated group, confirming its superior therapeutic effect (Figure 6e). In addition, the major organs (heart, liver, spleen, lung, and kidney) showed no damage, confirming the biosafety of the system (Figure 6e). These results demonstrate that PR-proC-Lipo induces tumor cell death via ROS-mediated lipid peroxidation and prodrug activation, thereby achieving enhanced antitumor efficacy *in vivo* with minimized systemic toxicity.

Conclusions

In summary, we have developed a tumor-targeted, liposome-mediated membrane fusion strategy that enables the stable anchoring of caged palladium nanoclusters (Pd NCs) within the plasma membrane, thereby addressing key limitations associated with metal NCs, including surface passivation and insufficient spatiotemporal control over ROS generation. Molecular cage-templated Pd NCs integrated into AS1411-functionalized liposomes exhibit efficient membrane fusion and sustained catalytic activity localized at the lipid bilayer. Within the confined membrane environment, Pd NCs display enhanced catalytic stability and efficiency, enabling robust *in situ* ROS production at substantially reduced metal dosages. The localized oxidative stress induces lipid peroxidation, disrupts membrane integrity, and modulates ferroptosis-related pathways, driving programmed cell death. In parallel, local ROS enables precise spatiotemporal activation of prodrugs and catalytic oxygen generation, thereby alleviating tumor hypoxia and enhancing therapeutic efficacy while minimizing off-target toxicity.

Beyond the specific Pd-based system demonstrated here, this work establishes membrane confinement via fusion as a generalizable strategy for integrating functional metal NPs into biological membranes for future study.

Author contributions

All authors contributed to writing of this manuscript.

Conflicts of interest

The authors declare no conflict of interest.

Data availability

The data supporting this study are available within the article and in the accompanying supplementary information (SI). Supplementary information is available.

Ethical Statement

All experimental procedures on mice were performed in compliance with the relevant laws and the Guidelines of Animal Experimental Ethics Committee of East China Normal University. All mice experiments have been approved by the committee (No. m20240802).

Acknowledgements

This work was financially supported by the Ministry of Science and Technology of China (2022YFA1505900 and 2024YFB3814900), National Natural Science Foundation of China (22202073), East China Normal University Multifunctional Platform for Innovation (004) and Fundamental Research Funds for the Central Universities.

References

1. Z. Liu, M. Sun, W. Zhang, J. Ren, X. Qu, *Target-Specific Bioorthogonal Reactions for Precise Biomedical Applications, Angew. Chem. Int. Ed.,* 2023, **62**, e202308396.
2. R. Zhang, X. Yan, K. Fan, *Nanozymes Inspired by Natural Enzymes, Acc. Mater. Res.,* 2021, **2**, 534–547.
3. Y. Wang, X. Jia, S. An, W. Yin, J. Huang, X. Jiang, *Nanozyme-Based Regulation of Cellular Metabolism and Their Applications, Adv. Mater.,* 2023, **36**, 2301810.
4. J. J. Soldevila-Barreda, N. Metzler-Nolte, *Intracellular Catalysis with Selected Metal Complexes and Metallic Nanoparticles: Advances toward the Development of Catalytic Metallodrugs, Chem. Rev.,* 2019, **119**, 829–869.
5. C. Gao, F. Lyu, Y. Yin, *Encapsulated Metal Nanoparticles for Catalysis, Chem. Rev.,* 2020, **121**, 834–881.

6. Y. Bai, J. Chen, S. C. Zimmerman, *Designed transition metal catalysts for intracellular organic synthesis, Chem. Soc. Rev.*, 2018, **47**, 1811–1821.
7. M. Yang, J. Li, P. R. Chen, *Transition metal-mediated bioorthogonal protein chemistry in living cells, Chem. Soc. Rev.*, 2014, **43**, 6511–6526.
8. J. Miguel-Ávila, M. Tomás-Gamasa, J. L. Mascareñas, *Metal-promoted synthetic chemistry within living cells, Trends Chem.*, 2023, **5**, 474–485.
9. E. Latocheski, G. M. Dal Forno, T. M. Ferreira, B. L. Oliveira, G. J. L. Bernardes, J. B. Domingos, *Mechanistic insights into transition metal-mediated bioorthogonal uncaging reactions, Chem. Soc. Rev.*, 2020, **49**, 7710–7729.
10. Y. Lu, W. Chen, *Sub-nanometre sized metal clusters: from synthetic challenges to the unique property discoveries, Chem. Soc. Rev.*, 2012, **41**, 3594–3623.
11. J. Y. Li, J. C. Wang, J. H. Zhou, K. Zhao, S. H. Liu, X. J. Zhao, S. L. Han, L. Y. Yao, J. K. Sun, *Spatiotemporal Regulation in Porous Organic Cage Salt–Metal Cluster Hybrids for Efficient Orthogonal Tandem Catalysis, Angew. Chem. Int. Ed.*, 2025, **64**, e202509941
12. S. Ren, L. Tan, J.-H. Zhou, J. Sun, P. Zhang, X. Cao, Y.-H. Zhang, J.-K. Sun, *Eco-Friendly Encapsulation of Metal Clusters in Porous Organic Cages for Engineerable Microenvironment and Enhanced Catalysis, CCS Chem.*, 2024, **6**, 2186–2197.
13. S.-Y. Zhang, Z. Kochovski, H.-C. Lee, Y. Lu, H. Zhang, J. Zhang, J.-K. Sun, J. Yuan, *Ionic organic cage-encapsulating phase-transferable metal clusters, Chem. Sci.*, 2019, **10**, 1450–1456.
14. J. Tang, C. Li, W. Ma, Z. Ba, Z. Hu, I. Willner, C. Wang, *An Activatable Caged Palladium Nanocomposite for Targeted Cancer Therapy, Angew. Chem. Int. Ed.*, 2025, **64**, e202503485.
15. X. Yang, J.-K. Sun, M. Kitta, H. Pang, Q. Xu, *Encapsulating highly catalytically active metal nanoclusters inside porous organic cages, Nat. Catal.*, 2018, **1**, 214–220.
16. D. Liu, C. Zhou, G. Wang, Y. Li, Z. Yang, C. Kong, B. Liu, *Active Pd nanoclusters supported on nitrogen/amino co-functionalized carbon for highly efficient dehydrogenation of formic acid, Chem. Synth.*, 2023, **3**, 24.
17. Q. Fu, C. Wei, M. Wang, *Transition-Metal-Based Nanozymes: Synthesis, Mechanisms of Therapeutic Action, and Applications in Cancer Treatment, ACS Nano,* 2024, **18**, 12049–12095.
18. S. Li, B. Xu, M. Lu, M. Sun, H. Yang, S. Liu, Z. Huang, H. Liu, *Tensile‐Strained Palladium Nanosheets for Synthetic Catalytic Therapy and Phototherapy, Adv. Mater.*, 2022, **34**, 2202609.
19. Z. Ye, Y. Fan, T. Zhu, D. Cao, X. Hu, S. Xiang, J. Li, Z. Guo, X. Chen, K. Tan, N. Zheng, *Preparation of Two-Dimensional Pd@Ir Nanosheets and Application in Bacterial Infection Treatment by the Generation of Reactive Oxygen Species, ACS Appl. Mater. Interfaces,* 2022, **14**, 23194–23205.
20. Q. Zhao, L. Zheng, Y. Gao, J. Li, J. Wei, M. Zhang, J. Sun, J. Ouyang, N. Na, *Dual Active Centers Linked by a Reversible Electron Station as a Multifunctional Nanozyme to Induce Synergetically Enhanced Cascade Catalysis for Tumor-Specific Therapy, J. Am. Chem. Soc.*, 2023, **145**, 12586–12600.
21. C. Ge, G. Fang, X. Shen, Y. Chong, W. G. Wamer, X. Gao, Z. Chai, C. Chen, J.-J. Yin, *Facet Energy versus Enzyme-like Activities: The Unexpected Protection of Palladium Nanocrystals against Oxidative Damage, ACS Nano,* 2016, **10**, 10436–10445.
22. X. Shen, W. Liu, X. Gao, Z. Lu, X. Wu, X. Gao, *Mechanisms of Oxidase and Superoxide Dismutation-like Activities of Gold, Silver, Platinum, and Palladium, and Their Alloys: A General Way to the Activation of Molecular Oxygen, J. Am. Chem. Soc.*, 2015, **137**, 15882–15891.
23. X. Wang, M. He, Y. Zhao, J. He, J. Huang, L. Zhang, Z. Xu, Y. Kang, P. Xue, *Bimetallic PtPd Atomic Clusters as Apoptosis/Ferroptosis Inducers for Antineoplastic Therapy through Heterogeneous Catalytic Processes, ACS Nano,* 2024, **18**, 8083–8098.
24. M. Chang, Z. Hou, M. Wang, C. Yang, R. Wang, F. Li, D. Liu, T. Peng, C. Li, J. Lin, *Single‐Atom Pd Nanozyme for Ferroptosis‐Boosted Mild‐Temperature Photothermal Therapy, Angew. Chem. Int. Ed.*, 2021, **60**, 12971–12979.
25. Z. Xi, X. Cheng, Z. Gao, M. Wang, T. Cai, M. Muzzio, E. Davidson, O. Chen, Y. Jung, S. Sun, Y. Xu, X. Xia, *Strain Effect in Palladium Nanostructures as Nanozymes, Nano Lett.*, 2019, **20**, 272–277.
26. C. Wang, Y. Li, W. Yang, L. Zhou, S. Wei, *Nanozyme with Robust Catalase Activity by Multiple Mechanisms and Its Application for Hypoxic Tumor Treatment, Adv. Healthcare Mater.*, 2021, **10**, 2100601.
27. H. Madec, F. Figueiredo, K. Cariou, S. Roland, M. Sollogoub, G. Gasser, *Metal complexes for catalytic and photocatalytic reactions in living cells and organisms, Chem. Sci.*, 2023, **14**, 409–442.
28. S. Fedeli, J. Im, S. Gopalakrishnan, J. L. Elia, A. Gupta, D. Kim, V. M. Rotello, *Nanomaterial-based bioorthogonal nanozymes for biological applications, Chem. Soc. Rev.*, 2021, **50**, 13467–13480.
29. C. C. James, B. de Bruin, J. N. H. Reek, *Transition Metal Catalysis in Living Cells: Progress, Challenges, and Novel Supramolecular Solutions, Angew. Chem. Int. Ed.*, 2023, **62**, e202306645.
30. T. Wu, Y. Chen, S. C. Zimmerman, H. Xing, Y. Bai, *Goals, challenges, and perspectives in chemical transformations within living systems, Cell Reports Phys. Sci.*, 2024, **5**, 101896.
31. J. W. Snyder, E. Skovsen, J. D. C. Lambert, P. R. Ogilby, *Subcellular, Time-Resolved Studies of Singlet Oxygen in Single Cells, J. Am. Chem. Soc.*, 2005, **127**, 14558–14559.
32. M. Ethirajan, Y. Chen, P. Joshi, R. K. Pandey, *The role of porphyrin chemistry in tumor imaging and photodynamic therapy, Chem. Soc. Rev.*, 2011, **40**, 340–362.
33. P. Zhan, A. Peil, Q. Jiang, D. Wang, S. Mousavi, Q. Xiong, Q. Shen, Y. Shang, B. Ding, C. Lin, Y. Ke, N. Liu, *Recent Advances in DNA Origami-Engineered Nanomaterials and Applications, Chem. Rev.*, 2023, **123**, 3976–4050.
34. Y. Zhong, L. Xu, C. Yang, L. Xu, G. Wang, Y. Guo, S. Cheng, X. Tian, C. Wang, R. Xie, X. Wang, L. Ding, H. Ju, *Site-selected in situ polymerization for living cell surface engineering, Nat. Commun.*, 2023, **14**, 7285.
35. F. Huang, J. Liu, M. Li, Y. Liu, *Nanoconstruction on Living Cell Surfaces with Cucurbit[7]uril-Based Supramolecular Polymer Chemistry: Toward Cell-Based Delivery of Bio-Orthogonal Catalytic Systems, J. Am. Chem. Soc.*, 2023, **145**, 26983–26992.
36. Y. Ma, Y. Zhou, J. Long, Q. Sun, Z. Luo, W. Wang, T. Hou, L. Yin, L. Zhao, J. Peng, Y. Ding, *A High‐Efficiency Bioorthogonal Tumor‐Membrane Reactor for In Situ Selective and Sustained Prodrug Activation, Angew. Chem. Int. Ed.*, 2024, **63**, e202318372
37. X. Feng, G. Tong, Z. Ran, X. Liu, L. Li, G. Liu, R. Yang, *Autocatalysis‐Integrated Bioorthogonal (Poly)Catalyst‐Linked Immunosorbent Assay for Living Cell*

Membrane Antigens, Angew. Chem. Int. Ed., 2024, **64**, e202417352

38. R. Qi, H. Zhao, X. Zhou, J. Liu, N. Dai, Y. Zeng, E. Zhang, F. Lv, Y. Huang, L. Liu, Y. Wang, S. Wang, *In Situ Synthesis of Photoactive Polymers on a Living Cell Surface via Bio-Palladium Catalysis for Modulating Biological Functions, Angew. Chem. Int. Ed.,* 2021, **60**, 5759–5765.
39. Y. Deng, T. Wu, X. Chen, Y. Chen, Y. Fei, Y. Liu, Z. Chen, H. Xing, Y. Bai, *A Membrane-Embedded Macromolecular Catalyst with Substrate Selectivity in Live Cells, J. Am. Chem. Soc.,* 2022, **145**, 1262–1272.
40. X. Wu, J. J. Hu, J. Yoon, *Cell Membrane as A Promising Therapeutic Target: From Materials Design to Biomedical Applications, Angew. Chem. Int. Ed.,* 2024, **63**, e202400249.
41. Y. Chen, T. Wu, S. Xie, Y. Bai, H. Xing, *Orientation-controlled membrane anchoring of bioorthogonal catalysts on live cells via liposome fusion–based transport, Sci. Adv.,* 2023, **9**, e2583.
42. Y. Ma, X. Liu, Q. Jiang, H.-D. Xu, G. Liang, W. Zhan, X. Sun, G. Liang, *Cell Membrane-Anchored Click Reaction Enhances Porphyrin Uptake for Highly Efficient Photodynamic Therapy of Breast Tumors, J. Am. Chem. Soc.,* 2025, **147**, 41657–41667.
43. Y. Chen, B. Chen, X. Zhou, C. Ren, R. Tang, M. Lin, Z. Nie, H. Xing, *Inner Leaflet-Anchored Multiplexed DNA Toolkits for Dynamic Tracking and Programmable Regulation of Cell Membrane Functions, J. Am. Chem. Soc.,* 2026, **148**, 4529–4543.
44. C. Liu, N. Yang, M. A. H. Nawaz, S. Song, W. Zhou, D. D. He, W. Han, Y. Li, C. Yu, *A Self-Reinforcing Nanozyme Platform for Synergistic Ferroptosis–Apoptosis Therapy via Amplified Reactive Oxygen Species Generation and Calcium Overload, ACS Appl. Nano Mater.,* 2025, **8**, 16694–16705.
45. Y. D. Yuan, J. Dong, J. Liu, D. Zhao, H. Wu, W. Zhou, H. X. Gan, Y. W. Tong, J. Jiang, D. Zhao, *Porous organic cages as synthetic water channels, Nat. Commun.,* 2020, **11**, 4927.
46. G. Fang, W. F. Li, X. M. Shen, J. M. Perez-Aguilar, Y. Chong, X. F. Gao, Z. F. Chai, C. Y. Chen, C. C. Ge, R. H. Zhou, *Differential Pd-nanocrystal facets demonstrate distinct antibacterial activity against Gram-positive and Gram-negative bacteria, Nat. Commun.,* 2018, **9**, 129.
47. C. Li, J. Tang, J. Tang, C. Wang, *Highly Catalytic Palladium Nanoclusters and Pd-Enzyme Composites as Catalytic Cascade Systems for Biosensing†, Chin. J. Chem .* 2025, **43**, 2457–2464.
48. B. Lim, M. Jiang, P. H. C. Camargo, E. C. Cho, J. Tao, X. Lu, Y. Zhu, Y. Xia, *Pd-Pt Bimetallic Nanodendrites with High Activity for Oxygen Reduction, Science,* 2009, **324**, 1302–1305.
49. L. Bai, W. Jiang, M. Sang, M. Liu, S. Xuan, S. Wang, K. C.-F. Leung, X. Gong, *Magnetic microspheres with polydopamine encapsulated ultra-small noble metal nanocrystals as mimetic enzymes for the colorimetric detection of H2O2 and glucose, J. Mater. Chem. B,* 2019, **7**, 4568–4580.
50. Y. Li, S. Li, M. Bao, L. Zhang, C. Carraro, R. Maboudian, A. Liu, W. Wei, Y. Zhang, S. Liu, *Pd Nanoclusters Confined in ZIF-8 Matrixes for Fluorescent Detection of Glucose and Cholesterol, ACS Appl. Nano Mater.,* 2021, **4**, 9132–9142.
51. M. Lin, Y. Chen, S. Zhao, R. Tang, Z. Nie, H. Xing, *A Biomimetic Approach for Spatially Controlled Cell Membrane Engineering Using Fusogenic Spherical Nucleic Acid, Angew. Chem. Int. Ed.,* 2021, **61**, e202111647.
52. F. Kong, Q. Lei, Y. Ma, P. He, G. Zheng, Y. Xu, J. Huang, C. J. Brinker, K. Liu, W. Zhu, *Membrane Fusion Liposome-Mediated Ferroptosis Explosion for Enhanced Cancer Therapy, Chem. Mater.,* 2023, **35**, 4731–4742.
53. Z. Fan, S. Wu, H. Deng, G. Li, L. Huang, H. Liu, *Light-Triggered Nanozymes Remodel the Tumor Hypoxic and Immunosuppressive Microenvironment for Ferroptosis-Enhanced Antitumor Immunity, ACS Nano,* 2024, **18**, 12261–12275.
54. J. Wang, M. Cao, L. Han, P. Shangguan, Y. Liu, Y. Zhong, C. Chen, G. Wang, X. Chen, M. Lin, M. Lu, Z. Luo, M. He, H. H. Y. Sung, G. Niu, J. W. Y. Lam, B. Shi, B. Z. Tang, *Blood–Brain Barrier-Penetrative Fluorescent Anticancer Agents Triggering Paraptosis and Ferroptosis for Glioblastoma Therapy, J. Am. Chem. Soc.,* 2024, **146**, 28783–28794.
55. Z. Yu, X. Xie, Q. Li, Y. Huang, S. Chen, W. Song, J. Tian, Z. Li, C. Wu, B. Li, *A Supramolecular Self-Assembled Nanoprodrug for Enhanced Ferroptosis Therapy, ACS Nano,* 2024, **18**, 32534–32546.
56. S. Zhang, X. Wu, X. Liao, S. Zhang, *Nanodrug Hijacking Blood Transferrin for Ferroptosis-Mediated Cancer Treatment, J. Am. Chem. Soc.,* 2024, **146**, 8567–8575.

View Article Online
DOI: 10.1039/D6SC02576E

Data availability

The data supporting this study are available within the article and in the accompanying supplementary information (SI). Supplementary information is available.